

Metal clusters on ultrathin oxide films: model catalysts for surface science studies

D.R. Rainer^{a,1}, D.W. Goodman^{b,*}

^a Akzo Nobel Chemicals, 13000 Bay Park Road, Pasadena, TX 77507, USA

^b Department of Chemistry, Texas A & M University, College Station, TX 77843-3255, USA

Received 18 June 1997; accepted 3 October 1997

Abstract

Characterization and reaction kinetics studies have been performed over a variety of planar model supported catalysts prepared by the vapor deposition of catalytically interesting metals onto ultrathin oxide films on refractory metal single crystal substrates in ultrahigh vacuum. These unique systems feature many of the advantages for fundamental study associated with single crystals, while addressing important issues for supported catalysts, such as the intrinsic effects of particle size and the role of the support. The oxide thin films have been shown to roughly mimic the chemical and physical properties of the bulk analogs, and yet they are electrically conductive via defects and tunnelling to the single crystal substrate. This renders them amenable to the various charged particle spectroscopies that comprise the core of modern surface science; also, because they are flat as well conductive, they are suitable for scanning-tunnelling and atomic force microscopy. Characterization studies carried out over these models focusing on structural, electronic, and chemical properties as a function of particle size have been related to parallel studies of relevant catalytic reactions, providing fundamental insight into these processes at the atomic level. The select group of experiments presented here provides a broad illustration of the versatility and utility of these materials for elucidating the properties of small, supported metal particles and for simulating catalysis over 'real world' high surface area supported catalysts. © 1998 Elsevier Science B.V.

Keywords: Ultrathin oxide films; Catalysts; Surface science

1. Introduction

At the core of heterogeneous catalysis research is the desire to correlate catalytic properties with the observed physical and structural properties of the catalyst at the atomic level. Many commercially important catalysts are comprised of catalytically active metals dis-

persed on high surface area oxide supports in order to maximize the metal surface area. The physical and chemical properties of small supported metal particles have been shown to be markedly size dependent [1,2]; in catalytic processes this is often manifested in size dependencies with regard to reaction activity and selectivity [3–7]. Therefore, in order to describe the fundamental dynamics of catalytic processes in these supported systems, a basic understanding of the properties of small, dispersed metal particles (< 1000 Å diameter) must first be achieved,

* Corresponding author. E-mail: goodman@chemvx.tamu.edu

¹ E-mail: drainer@wt.net

particularly those in the size regime below 50 Å.

The complexities of ‘real world’ supported catalysts render the prospect of obtaining a detailed comprehensive description of their microscopic properties from their exclusive study a rather delicate undertaking. The complications arising from porous, high surface area supports of poorly defined structure, uncertainty regarding metal particle size and morphology, and problems with surface contamination all serve to obscure a fundamental picture of the catalytic process at the most basic level. In the case of mixed metal systems, these difficulties are further exacerbated by added ambiguities concerning particle composition.

These types of difficulties have been addressed in the past by the employment of well-defined single crystal surfaces in coupled UHV-high pressure reactor systems [8,9]. This approach allows high pressure (up to a few Torr) kinetics studies to be combined with atomic level characterization of pre- and post-reaction catalyst surfaces, as well as in situ investigations. These studies have been instrumental in relating catalytic behavior with specific structure [10–18]. Numerous successes notwithstanding, there are certain shortcomings inherent in the employment of single crystals in the context of simulating catalytic processes over high surface area supported systems. Foremost among these are the exclusion of intrinsic particle size and support effects.

The desire for a model catalyst that more fully simulates all the important aspects of heterogeneous catalysis, and yet retains a certain tractability for fundamental study, has driven the development of the planar model supported catalyst as a sort of viable, complimentary intermediate to bridge the much publicized ‘material gap’ between single crystals and ‘real world’ catalysts. Because of their relative simplicity and suitability for study using UHV-based surface science characterization techniques, the employment of these unique materials serves as a means to circumvent much of the intrinsic

complexity associated with more conventional high surface area supported metal catalysts, while still allowing the important issues of intrinsic particle size effect and the role of the support to be addressed.

Another important feature of the planar model supported catalysts is their amenity to investigation using scanning-tunnelling and atomic force microscopies. Detailed, sometimes atomically resolved images can be acquired for these systems, illuminating aspects of particle morphologies and growth modes, interactions with the support, and basic electronic structure with a resolution and thoroughness that is really unimaginable for high surface area materials with the tools available now.

This review centers on the employment of planar model supported metal catalysts in coupled UHV-high pressure reactor systems as a means for studying heterogeneous catalytic processes. A diverse group of case studies has been selected for discussion that broadly illustrates some of the unique research opportunities afforded by these model systems.

2. Experimental

The coupled UHV-microreactor systems (base pressure $\sim 1 \times 10^{-10}$ Torr) employed in the experiments discussed here have been described in detail elsewhere in the literature [8,9]. The systems are variously equipped with an array of surface science techniques including Auger electron spectroscopy (AES), temperature programmed desorption (TPD), low-energy electron diffraction (LEED), ion scattering spectroscopy (ISS), X-ray and ultraviolet photoelectron spectroscopy (XPS and UPS), high resolution electron energy loss spectroscopy (HREELS), in situ infrared reflection absorption spectroscopy (IRAS), transmission electron microscopy (TEM), and UHV-STM and AFM.

Detailed treatments of the experimental aspects of thin film deposition are available in the literature [19–22], and only the most basic ele-

ments of this aspect of model catalyst preparation will be discussed here. Typically, oxide thin films were obtained by vapor depositing the desired metal (Al, Si, Mg, Ni, or Ti) onto a refractory metal single crystal substrate in a background pressure of O_2 ($\sim 1 \times 10^{-6}$ Torr) under prescribed annealing conditions. Oxide film thicknesses were determined from the attenuation of the XPS or AES substrate signal. Film stoichiometry and order were monitored using AES, XPS, EELS, and LEED. For the TEM samples, Al_2O_3 films were deposited in an identical manner onto carbon covered molybdenum TEM grids.

Supported metal particles in the model systems were obtained by vapor deposition in UHV, accomplished by evaporation through the resistive heating of high purity wires of the desired metals. Particle size distributions and growth modes were influenced by total metal coverage, and deposition and annealing substrate temperature. Sample temperatures were monitored with

a type 'C' thermocouple spot-welded to the edge of the single crystal substrate.

The reaction kinetics experiments over the single crystal and planar model supported catalysts were carried out in the batch reaction mode in UHV-microreactor systems (described above) using gas chromatography or gas phase IR spectroscopy to analyze the products. The CO + NO reactions over Pd/ Al_2O_3 powders were carried out in the steady state flow mode in a conventional plug flow reactor.

3. Results and discussion

3.1. Thin film supports

Several thorough discussions of the unique properties of oxide thin films (20–100 Å) supported on refractory metal single crystal substrates in UHV appear in the literature [19–22]; since this review deals primarily with the prop-

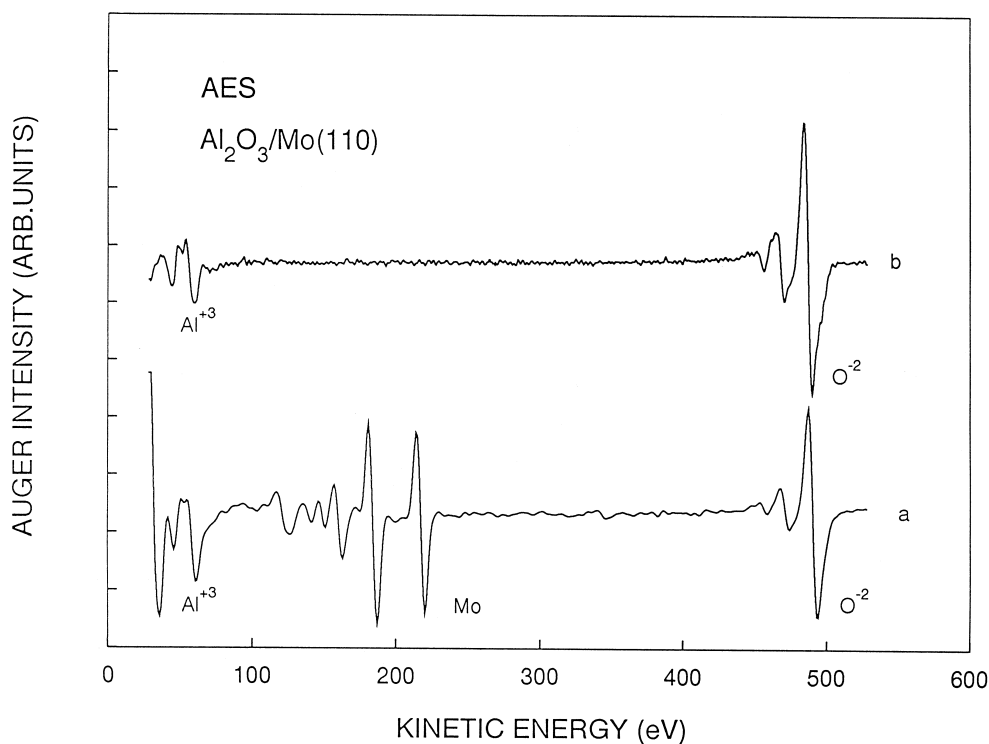


Fig. 1. AES of Al_2O_3 films on Mo(110) of thickness 4.4 Å (a) and 20 Å (b) [23].

erties of the supported metals, only a cursory overview of oxide thin film properties will be presented here.

Fig. 1 shows the Auger spectra for two Al_2O_3 films on Mo(110) grown in a 7×10^{-7} Torr background pressure of O_2 at 900 K at a deposition rate of ~ 0.5 ML/min, followed by flash annealing to 1200 K in the O_2 ambient to improve the crystalline quality. The thickness of the 4.4 Å film was calculated from the AES intensity ratio of the Al^{3+} (LVV) peak to the Mo (MNN) peak. The thickness of the 20 Å film was extrapolated based on evaporation time at constant Al flux. For the 20 Å film, no Mo features appear in the spectrum, indicating that the single crystal substrate is effectively covered, consistent with analogous ISS findings [24]. For each spectrum, the dominant Al feature appears at ~ 54 eV, attributed to Al in the 3+ oxidation state; there is no evidence for the presence of metallic Al, indicating a stoichiometrically pure Al_2O_3 film within detection limits. In fact, with repeated exposures to the 2000 eV electron beam, one can observe an Al^0 feature at 68 eV that appears and grows in real time as Al is reduced by the effect of the beam [23].

XPS studies of thin SiO_2 films supported on Mo(100) have likewise shown that under the proper deposition conditions, films of 99% stoichiometric purity can be achieved [25]. Additionally, EELS studies yield spectra that are qualitatively identical to analogous results for bulk vitreous silica [26,27]. Similarly, IRAS experiments have indicated that the same type of ordering can be induced in these films as is observed for the bulk material [28]. These representative examples, selected from a much larger body of experiments over several oxide materials, indicate the suitability of thin oxide films as relevant model supports.

Summarizing the most salient features of the oxide thin films for their employment in this role, we can say that the films are thick enough to roughly mimic the physical and chemical properties of the bulk analogs, and yet thin

enough to be electrically conductive via defects and tunnelling to the single crystal substrate. This allows the various charged particle spectroscopies of UHV-based surface science to be applied without the attendant charging problems normally associated with insulating materials, and also renders the sample suitable for STM study. Additionally, thermal conductivities are not a problem with these ultrathin films in intimate contact with macroscopic metal substrates, which avoids the thermal gradients that occur across bulk insulators upon rapid heating, a significant advantage in temperature controlled experiments, particularly TPD. All of the films have been shown to be thermally stable at least up to temperatures of 1200 K.

3.2. Physical characteristics of supported metal particles in planar model supported catalysts

3.2.1. Size distribution

In any study concerned with small supported metal particles, the determination of particle size is a critical issue. A common approach is through the quantitative chemisorption of an adsorbate molecule (CO , H_2 , etc.), essentially titrating the number of available surface atoms, and making an assumption about particle shape to extract a single average particle size for the entire sample. This method is limited in that it provides no information regarding the width or shape of the overall particle size distribution. Also, adsorbate packing densities can change with particle size, especially for very small particles, introducing an error into surface area and size determinations by this method. A similar method entails using the rate of a structure insensitive reaction as an indication of exposed metal surface area. The CO oxidation rate over $\text{Pd}/\text{Al}_2\text{O}_3$ powder catalysts was used to measure the dispersion of the supported Pd. This reaction has been shown to be structure insensitive by comparative studies over single crystal, high surface area supported, and planar model supported Pd catalysts [7,29,30].

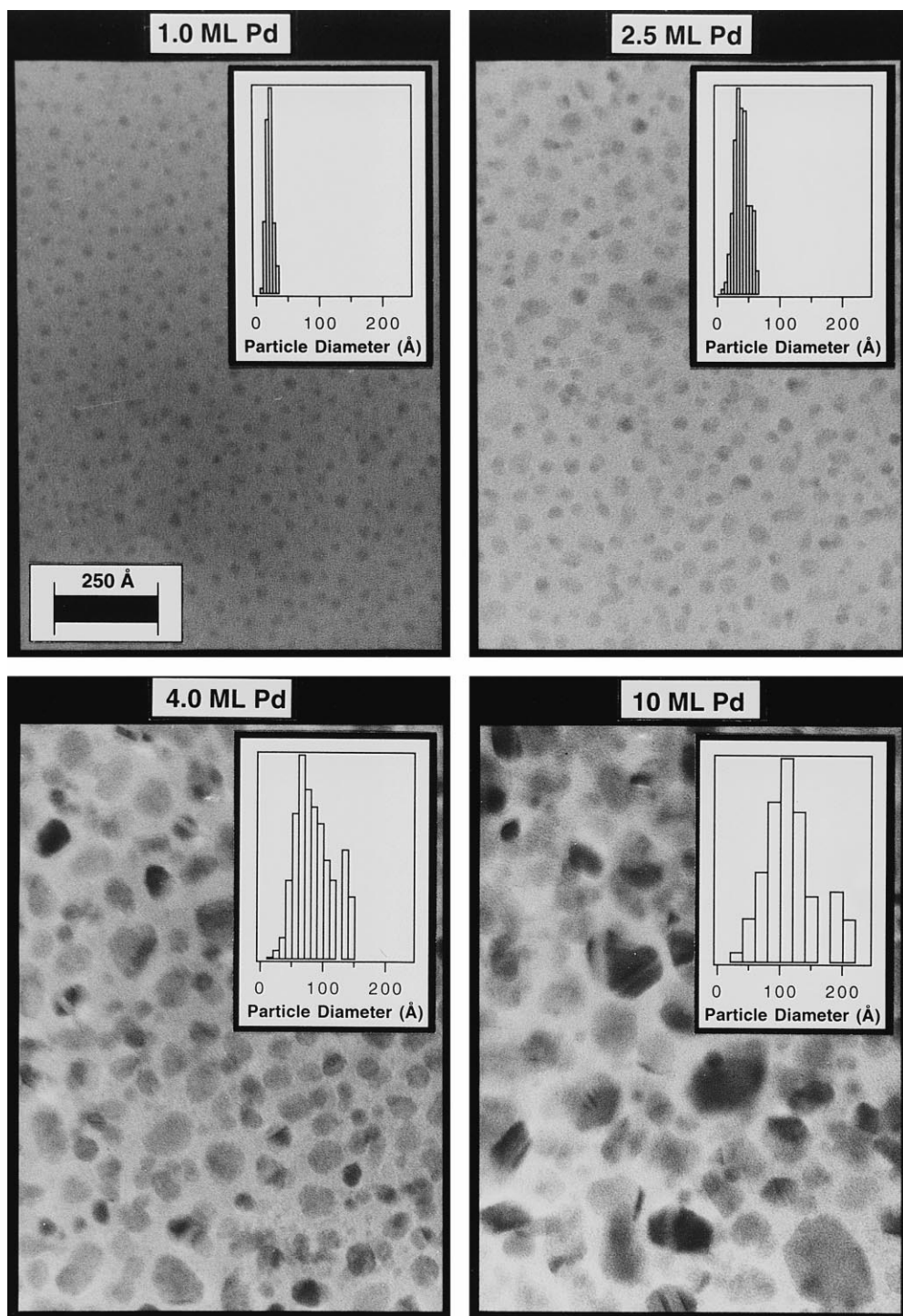


Fig. 2. TEM images for Pd/Al₂O₃(30 Å)/C samples for the indicated Pd coverages deposited at 500 K and flash annealed to 800 K. The particle size histograms are inset for each micrograph [31].

An alternative approach to these methods that rely solely on the quantification of metal surface area, is through the employment of a direct imaging technique such as TEM, STM, or AFM, providing a more detailed perspective of the overall particle size distribution. Care must be

taken, however, to insure that the imaged area is in fact representative of the entire sample since only a fraction of a percent of total surface area can be investigated in this way. Fig. 2 shows TEM micrographs for four different coverages of Pd in specially prepared Pd/Al₂O₃/C sam-

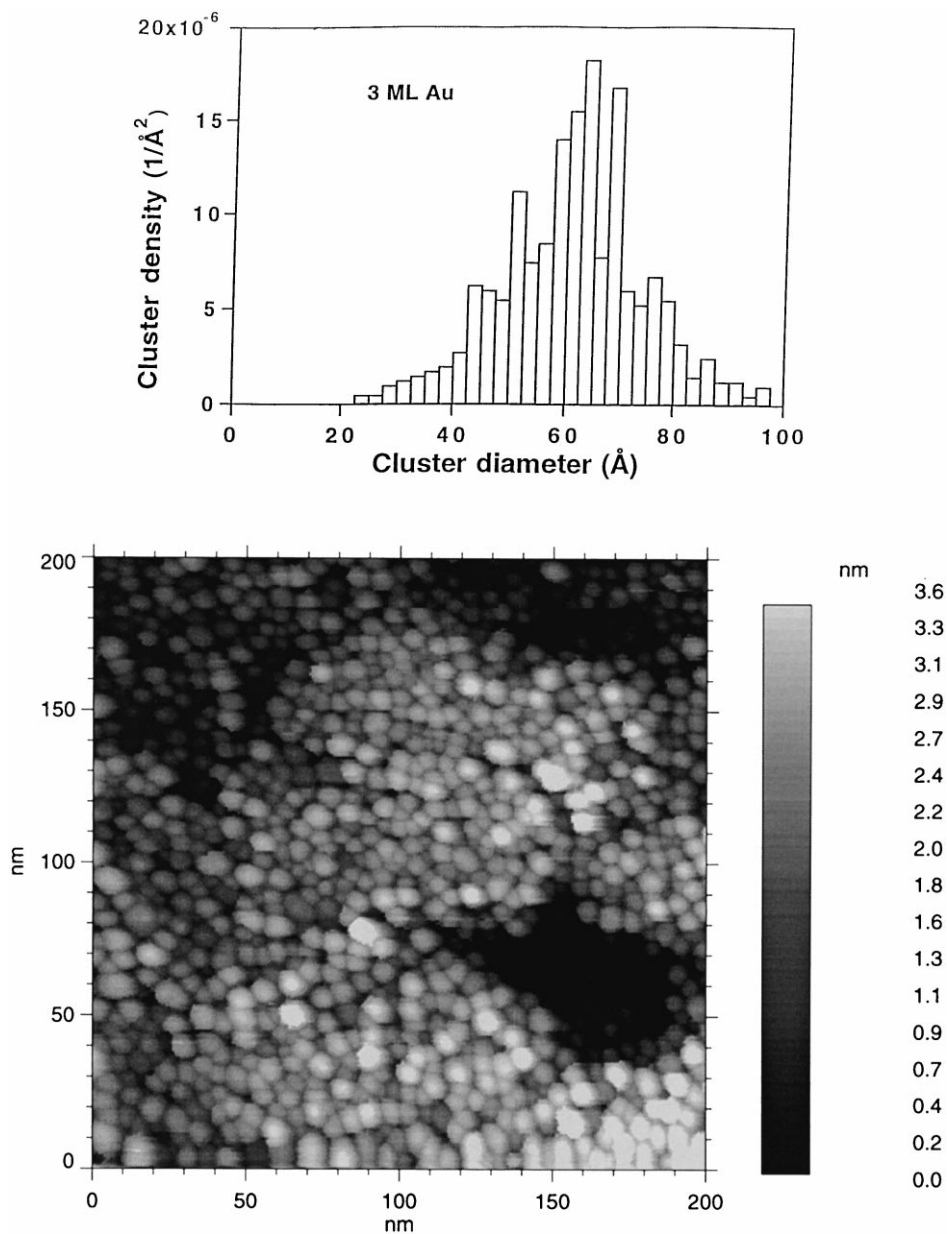


Fig. 3. STM of Au(3.0 ML)/TiO₂(30 ML)/Mo(100): (a) 2000 \times 2000 \AA micrograph, (b) particle size histogram [33].

ples supported on Mo TEM grids, with the corresponding particle size histograms inset. The Pd was deposited at a substrate temperature of 500 K, and subsequently flash annealed to 800 K. The histograms reveal fairly narrow particle size distributions of uniform, gaussian shape; multiple measurements acquired from various regions of the samples, indicate that each image is quite representative of the entire surface [31]. Comparisons with analogous Pd films deposited at 300 K and unannealed, not shown, reveal distinct differences in the particle growth mode, manifested as differences in the number density and average size and shape of the particles [32].

STM can also be used to acquire particle size data, and features the added benefit of providing information in the 'z' (normal to the surface) direction. An STM image of a Au(3.0 ML)/TiO₂(30 ML)/Mo(100) model catalyst is presented in Fig. 3, along with the associated particle size histogram, revealing a fairly narrow particle size distribution of flattened hemispherical clusters with an average diameter of 62 Å and average height of 16 Å [33]. However, a simple calculation comparing the amount of material deposited with the observed cluster density and particle size distribution reveals that the STM significantly overestimates the Au coverage. This is a consistent finding for STM particle size determinations, and reflects the intrinsic error associated with the STM in this role. This inherent size overestimation stems from two primary sources. First is the convolution error arising from the non-ideality of the tip, which broadens the imaged features, and makes the particles appear larger than they really are. Second, the high density of states in the Au clusters relative to the TiO₂ support leads to an enhancement of the apparent particle size, particularly in the 'z' dimension [33].

Clearly, these two basic methods (active metal surface area measurement vs. direct imaging) complement each other and the most thorough approach to particle size analysis entails applying them in tandem. For the majority of systems discussed here, the particle sizes referred to

have been determined by direct imaging techniques, often with corroboration from independent surface area measurements.

3.2.2. Structure—monometallics

Infrared spectroscopic studies of model supported catalysts can provide detailed structural and chemisorptive information; IRAS using CO as a probe molecule represents a very powerful approach to the investigation of the surface morphologies of small supported metal particles. CO stretching frequencies can be related to specific binding sites on the surface and comparisons with single crystal IR results can provide qualitative indications of the relative facet distribution on the surface of the particles. This type of characterization is particularly valuable in relating reaction kinetics data for supported catalysts to analogous results acquired over single crystals.

Fig. 4 shows IRAS spectra for three different coverages of Pd in a Pd/Al₂O₃/Mo(110) cata-

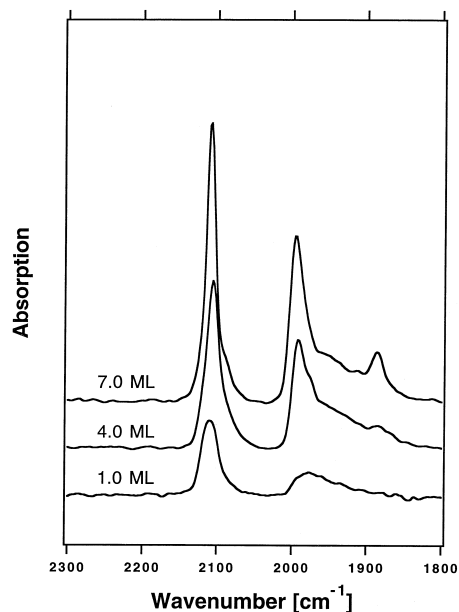


Fig. 4. IRAS of chemisorbed CO on Pd/Al₂O₃/Mo(110) at 110 K in 1.5×10^{-6} Torr CO at the indicated Pd coverages. The coverages correspond to the following average Pd particle sizes based on comparisons with TEM work: (7 ML: ~ 80 Å, 4 ML: ~ 50 Å, 1 ML: ~ 25 Å).

lyst. For the 7.0 ML Pd coverage (corresponding to an average particle size of ~ 100 Å based on the TEM images), four absorbance features are apparent in the CO spectrum at 110 K. The features at 2110, 1990, and 1880 cm^{-1} have been attributed to CO bound in the linear atop, two-fold bridging, and three-fold hollow sites respectively based on single crystal comparisons [34,35]. This combination of peaks is suggestive of a high concentration of $\langle 111 \rangle$ facets; in fact, an IRAS annealing series for these particles reveals a very specific coverage driven phase transition in the compressed CO overlayer associated with the Pd(111) surface [35,36]. Additionally, the peak at 1998 cm^{-1} is suggestive of CO bound in the two fold bridging site on the $\langle 100 \rangle$ facet. These simple comparisons seem to indicate that the morphologies of the 100 Å particles are dominated by low index $\langle 111 \rangle$ and $\langle 100 \rangle$ type faceting, though by no means completely excluding the presence of other faces [36]. These results have been supported by similar findings in previous IR experiments over planar model supported Pd/SiO₂ [37] and weak field dark beam imaging of Pd/MgO catalysts [38]. Of course, based on thermodynamic considerations alone, this is what one would expect to observe.

As the coverage (and average particle size) decrease, instructive changes occur in the absorption spectra reflecting structural changes in the particles. For one thing, the ratio of linear atop to multiply-bound CO intensity is increasing. This is suggestive of a higher density of low-coordinated, step/edge defect sites, again providing spectroscopic evidence of a fairly intuitive result, considering the increased ratio of facet edges for smaller particles of constant shape. A second observation is that the features become broader and less well resolved as the particles get smaller. This can be interpreted in a couple of ways. The obvious implication is that the smaller particles exhibit less well defined faceting, exhibiting a greater degree of structural heterogeneity resulting from the enhanced influence of the metal-support interac-

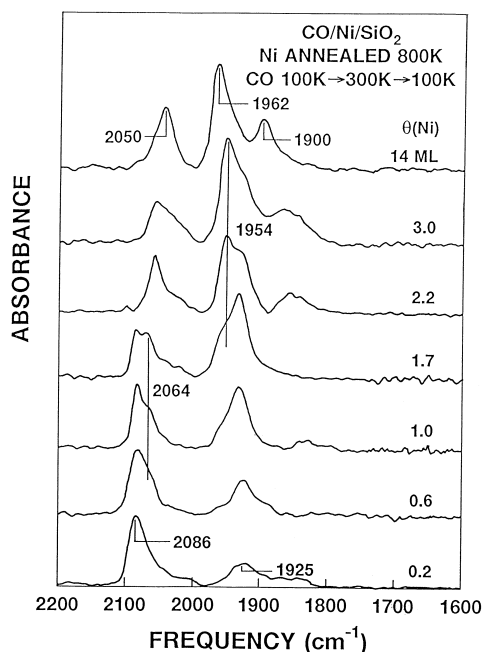


Fig. 5. IRAS of chemisorbed CO on Ni/SiO₂/Mo(110) at 100 K at the indicated Ni coverages [39].

tion with increasing dispersion. Another explanation is that the enhanced curvature associated with particles of diminishing size precludes the kind of compression required to induce the long range order in the overlayer associated with CO bound on large terraces [36].

Similar results have been observed for Ni. Fig. 5 displays IRAS spectra for CO adsorbed on Ni in the Ni/SiO₂/Mo(110) catalyst at several different Ni coverages. The spectra for the largest particles are dominated by features (or patterns of features) associated with low index $\langle 111 \rangle$ and $\langle 100 \rangle$ facets, while the smallest particles exhibit a high ratio of linear atop to multiply-bound CO intensity [39]. These results will be relevant in the ensuing discussions concerning reaction kinetics over these model systems.

Clearly IRAS provides valuable structural information for supported monometallic particles. The experiments described below show that the method can also be applied to supported bimetallics.

3.2.3. Surface composition—bimetallics

Supported mixed metal catalysts have elicited considerable interest for decades, due to their enhanced catalytic properties and importance in a variety of commercial processes. One of the primary difficulties associated with the study of small, supported bimetallic particles is the uncertainty regarding the elemental composition at the particle surface. For certain combinations of metals, IRAS studies using CO as a probe molecule over planar model supported bimetallic catalysts yields qualitative information regarding surface composition.

Because Cu and Pd display significantly different adsorption properties for CO, certain absorbance features can be identified with a par-

ticular metal. For example, since Cu only binds CO in the linear atop site (exhibiting a stretching frequency between 2050 and 2110 cm^{-1} [40–42]), any multiply-bound CO features appearing in the spectrum are most likely attributable to CO bound on Pd, barring dramatic ligand effects or mixed metal binding sites. No evidence for either of these was apparent in the experiment described below [42].

An annealing series for a Cu(1.0 ML)/Pd(7.0 ML)/Al₂O₃/Mo(100) model catalyst in a 2×10^{-6} Torr CO background is presented in Fig. 6. The Pd was deposited at 500 K, with subsequent annealing to 800 K, followed by a 1.0 ML deposition of Cu at 120 K. At 105 K, two features appear in the spectrum. The dominant

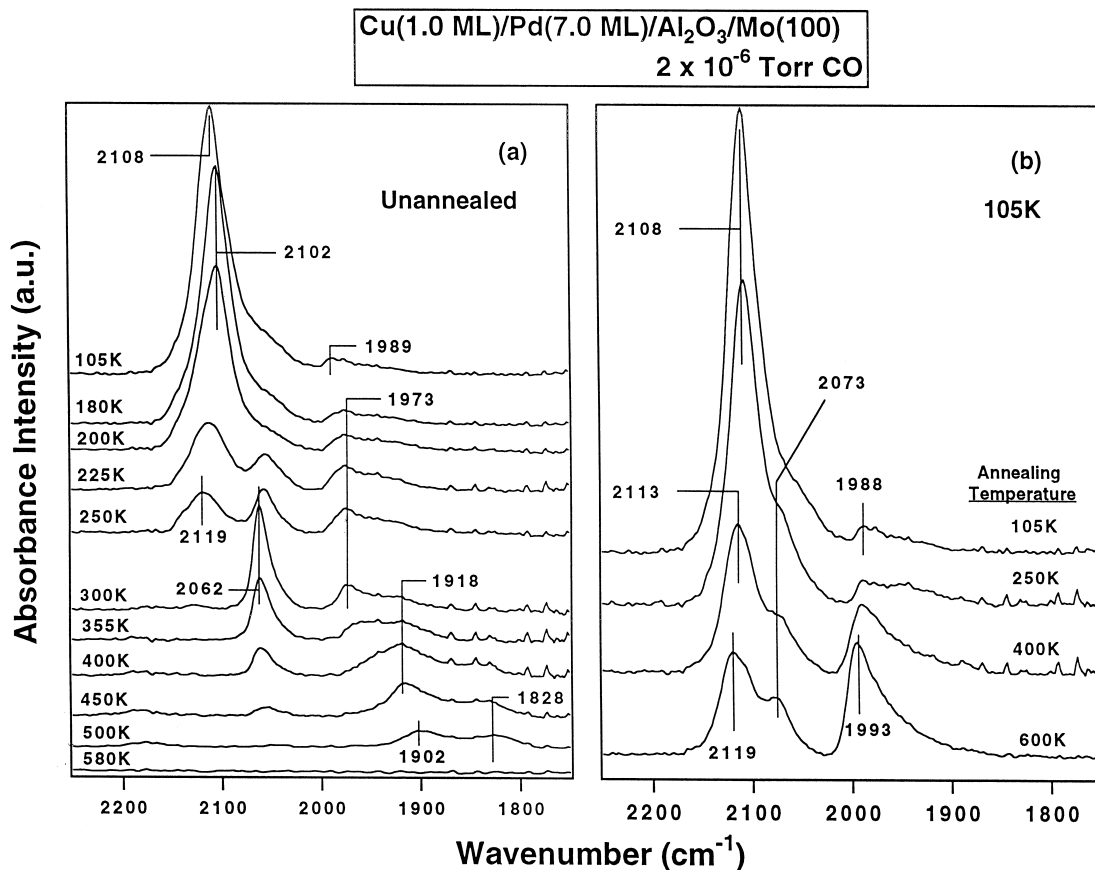


Fig. 6. (a) IRAS annealing series for CO on Cu(1.0 ML)/Pd(7.0 ML)/Al₂O₃/Mo(100) in a CO background pressure of 2×10^{-6} Torr. The Pd was deposited at 500 K and flash annealed to 800 K, followed by deposition of Cu at 120 K with no annealing prior to initial CO exposure. (b) IRAS spectra at 105 K for the same catalyst after annealing to 105 K, 250 K, 400 K, and 600 K in a 2×10^{-6} Torr CO background [42].

peak appears at 2108 cm^{-1} , corresponding to CO bound in the atop position on Cu and/or Pd, with a very small additional feature at 1989 cm^{-1} , in the region normally associated with CO adsorbed on Pd in a bridge-bound position. Clearly, this feature is dramatically attenuated compared to the pure Pd catalyst in Fig. 5. This is consistent with Cu effectively wetting the surface of the Pd to the degree that relatively few Pd atoms exist side by side in the surface layer. Similarly, there is no feature for CO bound in the three-fold hollow site.

As the sample is annealed in CO, several changes are apparent in the spectrum. At 225 K, the peak in the Pd bridge-bound region starts to intensify slightly. Also, a new peak appears at $\sim 2060\text{ cm}^{-1}$, being fully attenuated by $\sim 450\text{ K}$. The origin of this peak is not immediately obvious; it is improbable that it is related to CO bound on Cu, because the temperature range over which it is observed is too high (based on comparisons with an analogous annealing series on monometallic Cu catalysts [42]). Previous studies by Bertolini et al. [97] on well mixed Cu–Pd alloys indicate only a modest increase in the heat of adsorption of CO on Cu due to the electronic interaction with Pd, insufficient to account for the difference noted here in the thermal stability if the feature at 2060 cm^{-1} was in fact related to CO bound on electronically modified Cu.

As for the possibility that the feature is related to a mixed metal binding site, the stretching frequency is far too high to be associated with multiply-bound CO. Additionally, HREELS studies of CO bound on the Cu{001}c(2 × 2)–Pd surface (a well-ordered 50%–50% Cu–Pd alloy surface) by Lu et al., provided no indications of CO simultaneously bound to both Cu and Pd [43].

Comparisons with pure Pd model supported catalysts and the Pd(111) single crystal may yield some insight into the origin of this feature. For similar annealing series over larger Pd particles ($> \sim 50\text{ \AA}$) in Pd/Al₂O₃/Mo(110) and over the Pd(111) single crystal, a peak that has

been associated with atop-bound CO in an uncompressed overlayer appears at about 2075 cm^{-1} and demonstrates virtually identical thermal behavior as the peak at 2060 cm^{-1} in the bimetallic [36]; however, for the bimetallic, the peak is sharper, and more intense relative to the other peaks in the spectrum. A similar IRAS feature at 2065 cm^{-1} for CO bound on a 75% Pd(Cu)/SiO₂ powder catalyst in a study by Hendrickx and Poncic has likewise been attributed to CO bound atop on Pd [44]. Similar studies performed on the Cu(1.0 ML)/Pd(1.0 ML)/Mo(110) system, which ISS studies have shown to exist as discrete monolayers at room temperature with thermally induced mixing at higher temperatures [45], have revealed the same feature at $\sim 2060\text{ cm}^{-1}$, increasing in intensity with increasing Pd on the surface and demonstrating similar thermal behavior [46]. Thus, though the stretching frequency is $10\text{--}15\text{ cm}^{-1}$ lower in the bimetallics than that observed at similar temperatures on the pure Pd catalyst, this feature appears to be related to CO bound linear atop on Pd. The enhanced intensity can be rationalized in terms of an enhancement in the coverage of the uncompressed CO bound atop on Pd due to a dilution in the concentration of Pd atoms in the surface layer by Cu, an ensemble effect; in the analogous pure Pd work over the (111) single crystal surface and the model supported catalysts, most of the intensity resides in the multiply-bound CO at these temperatures [35,36]. The frequency redshift of this feature relative to that observed for the single crystal and the pure Pd model supported catalyst could be a result of either a reduction in the dipole–dipole interaction of CO or an electronic modification of Pd by Cu that alters the Pd–CO bond.

Fig. 6b shows the IRAS spectra for the same sample at saturation coverages of CO at 105 K after the sample has been annealed to successively higher temperatures in the CO background and re-cooled. The unannealed sample and the sample annealed to 250 K display only slight differences, but for the 400 K annealing

temperature, notable changes have occurred. The Pd bridge-bound peak has increased significantly, the high frequency atop feature has decreased, and a shoulder at approximately 2060 cm^{-1} has appeared. The emergence of the Pd bridge-bound peak indicates an increasing concentration of Pd on the surface. As the annealing temperature is further increased to 600 K, the ratio of the Pd bridge-bound to the atop feature also increases. Again, these results are consistent with ISS results for Cu deposited on multilayer Pd films supported on Mo(110) that indicate significant Cu diffusion into the bulk Pd as the annealing temperature is increased in a similar range [45]. The appearance of the shoulder at 2060 cm^{-1} at 105 K is again sug-

gestive of CO bound atop on Pd atoms relatively dispersed in a Cu surface in such a way as to preclude the formation of the compressed CO overlayer. The large peak widths probably result from the increased inhomogeneity that one would expect in a well mixed, disordered alloy.

Fig. 7a shows a CO annealing series for a Pd(1.0 ML)/Cu(6.0 ML)/Al₂O₃/Mo(100) catalyst. The deposition order for this catalyst was reversed; the Cu was deposited at 500 K and annealed to 600 K, followed by Pd deposition at 120 K with no annealing prior to CO exposure. At 105 K, the spectrum looks very similar to that of a pure 1.0 ML Pd catalyst (see Fig. 5) [36], with a large peak in the region associated

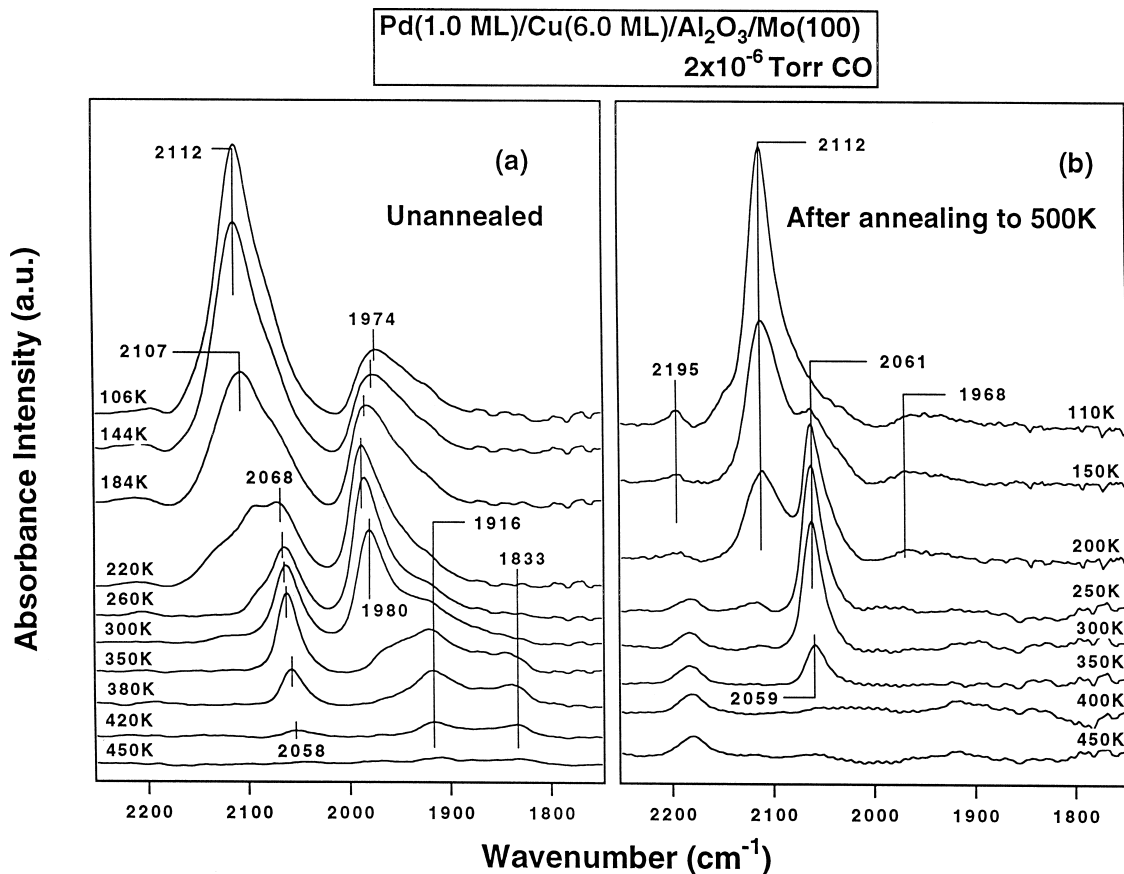


Fig. 7. IRAS annealing series for a Pd(1.0 ML)/Cu(6.0 ML)/Al₂O₃/Mo(100) catalyst in a 2×10^{-6} Torr CO background for (a) the unannealed catalyst and (b) the same catalyst after annealing in CO to 500 K. The Cu was deposited at 500 K and flash annealed to 600 K, followed by Pd deposition at 120 K with no annealing prior to initial CO exposure [42].

with atop bound CO ($\sim 2112\text{ cm}^{-1}$) and a smaller peak in the bridge-bound region (1974 cm^{-1}). The peaks for the unannealed saturation coverage are broad, again suggestive of a poorly ordered surface and possibly also due to disorder in the CO overlayer that results from the low temperature initial adsorption conditions [35,36]. As the sample is annealed, an intensity shift from the high frequency atop peak to a peak at $\sim 2060\text{ cm}^{-1}$ begins at 220 K. By 300 K a single peak at 2065 cm^{-1} can be seen in this frequency region, in addition to the lower energy peaks attributed to CO multiply-bound on Pd at 1980 and 1920 cm^{-1} . At 350 K, three features are evident at 1974 , 1920 , and 1840 cm^{-1} , associated with bridge- and three-fold hollow-bound CO. By 450 K, these multiply-bound CO peaks have almost been completely attenuated. Since these features persist in the spectrum at temperatures up to $\sim 550\text{ K}$ on pure Pd catalysts, this indicates that the concentration of Pd on the surface is decreasing with heating due, again, to diffusion of the admetal into the bulk dissimilar metal onto which it has been deposited. This is consistent with ISS results for Pd adsorbed on multilayer Cu on Mo(110) that indicates significant diffusion of surface Pd into the Cu film has occurred at an annealing temperature of 500 K for Pd deposited at 325 K [45].

A second temperature series for the same catalyst, after annealing in CO to 600 K, is presented in Fig. 7b. At 110 K, the peak at 2112 cm^{-1} has narrowed significantly, indicative of the different initial adsorption conditions, and possibly of a decrease in the heterogeneity of the binding sites relative to the unannealed sample. The peak intensity for the bridge-bound CO has been attenuated dramatically, which is consistent with thermally stimulated Pd diffusion into the Cu particles. In fact, throughout this entire post-annealed temperature series, no features associated with multiply-bound CO on Pd are apparent.

As the temperature is increased, the peak at 2112 cm^{-1} is attenuated, demonstrating thermal

stability consistent with the atop feature observed on the pure Cu catalyst. Concurrently, a feature at 2061 cm^{-1} appears and grows in intensity, virtually identical to the corresponding feature in the Cu(1.0 ML)/Pd(7.0 ML)/Al₂O₃/Mo(100) catalyst. Again, this peak must be related to Pd, as the thermal stability is too high for CO on Cu, though the peak position is shifted slightly relative to the uncompressed atop CO feature on the pure Pd catalysts.

The IRAS results for these Cu–Pd/Al₂O₃/Mo(100) catalysts illustrate how this technique can be used to at least qualitatively address surface composition in mixed metal catalysts. For the most part, the spectra for the bimetallics exhibited a straightforward combination of the same features observed for the two monometallic catalysts. Information regarding the relative degree of metal mixing at the surface and the degree of alloying is clearly provided by CO binding configurations and thermal behavior. For both of these catalysts, in the temperature range from $\sim 200\text{ K}$ to $\sim 400\text{ K}$, a sharp peak possibly attributable to CO bound atop on isolated Pd in a mixed Pd–Cu surface is evident in the spectrum. Similar results for Au–Pd systems lend support to this interpretation [42].

3.2.4. Electronic properties

Certain electronic modifications are expected to occur with changing particle size, arising from the attendant changes in average metal atom coordination number, particularly in the limit of very small particles. In recent years, these size dependent intrinsic electronic effects have been accorded a great deal of interest, both for the implications for heterogeneous catalysis and from a broader materials science perspective. A common approach has been the investigation of supported model catalysts using photoelectron spectroscopies (XPS to monitor core level modifications and UPS for changes in the valence band); a variety of supported metal systems have been studied in this fashion, yield-

ing insight into electronic modifications stemming from both intrinsic particle size effects and influences from the support [47–54]. The expected crossover from metallic to non-metallic behavior has garnered particular interest [47].

XPS and TPD results for the Cu/SiO₂/Mo(110) catalyst are presented as a function of Cu coverage (and hence particle size) in Fig. 8. Fig. 8a and b depict the core level binding energy (CLBE) and the peak width for the Cu 2p_{3/2} transition, while Fig. 8c presents the energy of sublimation of the supported Cu determined by leading edge analysis of TPD data. For each of the three properties, a transition from a distinct particle size dependence to a constant bulk value is observed between a 1.0

and 2.0 ML coverage. Based on chemisorption experiments, this corresponds to an average particle size somewhere between ~20 and 25 Å, assuming hemispherical shape (remembering that there will be a significant fraction of even smaller particles in the lower end of the size distribution) [55]. There are several ways that this could be interpreted. The observed changes could reflect an enhancement in the contribution from the metal support interaction with decreasing particle size (CuO displays a higher CLBE and a broader peak width), a change in the particle growth mode at some critical coverage, or perhaps the transition from non-metallic to metallic behavior.

While XPS and UPS studies of the electronic structure of supported particles has been shown to be an interesting and practical approach, interpretation of results can be problematic, particularly in terms of separating initial state and final state effects. The correlation demonstrated above between the XPS results and the sublimation energy suggests that initial state effects are more important in this particular example, but that is by no means conclusive. Also, typical experiments of these types yield information averaged across some range of particle sizes, such that differences arising from subtle variations in size and shape are difficult to resolve.

Scanning-tunnelling spectroscopy (STS) using UHV-based STM allows for the investigation of the electronic properties of a particular particle to be undertaken. This removes the ambiguity regarding particle size and shape and allows the investigation to proceed in a very localized and focused way; a specific feature in the real time micrograph can be pointedly selected and studied. The STS technique entails varying the bias voltage on the STM tip and measuring the tunnelling current, generating an *I*–*V* curve that provides an indication of the density of states in the region of the Fermi level.

An STM topographical image for 1.2 ML Pd deposited on a 30 ML MgO film on Mo(100) is presented in Fig. 9, along with *I*–*V* curves

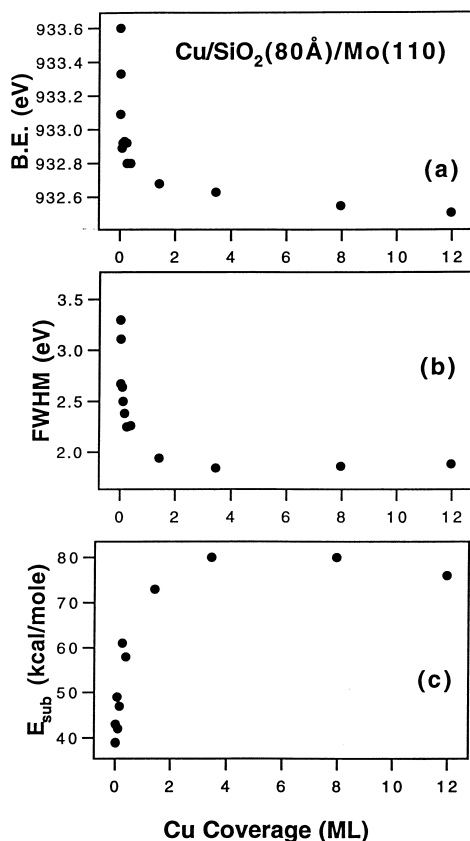


Fig. 8. Coverage (particle size) dependencies for the following properties in a Cu/SiO₂/Mo(100) catalyst: (a) CLBE of the Cu 2p_{3/2} transition, (b) FWHM of the Cu 2p_{3/2} peak, and (c) energy of sublimation of the Cu particles as determined by leading edge analysis of TPD data [32].

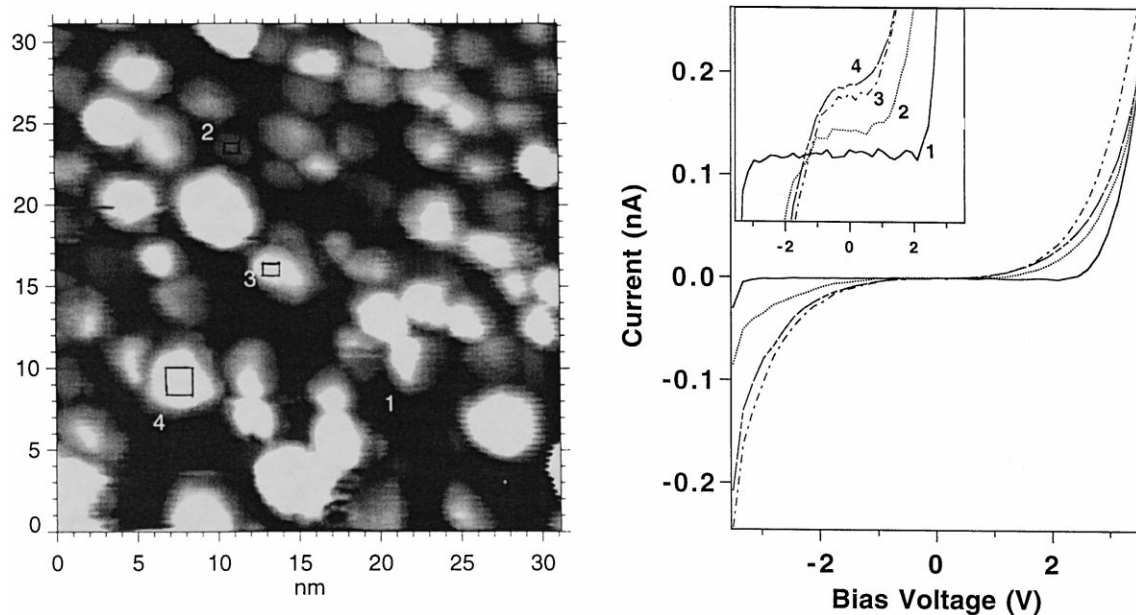


Fig. 9. Scanning-tunneling micrograph of Pd(1.2 ML)/MgO(100)/Mo(100) with corresponding STS acquired at the indicated regions on the surface (boxes 1, 2, 3, and 4) [33].

corresponding to the regions specified in the micrograph. The inset provides an expanded view with the I - V curves offset from one another for the sake of clarity. Curve 1 is measured from the MgO film itself. A band gap of 5.5 eV is apparent in the STS, in good agreement with the surface bandgap measured for MgO using EELS [56]. The other three STS measurements were acquired from particles 2, 3, and 4 with the following apparent dimensions (remembering that measurements made with STM tend to overestimate the size of the particles, as previously discussed): 13 Å diameter \times 6 Å height, 22 Å \times 10 Å, and 38 Å \times 16 Å, respectively. For particle 4, the largest particle in the set, no band gap is evident; the particle clearly exhibits metallic character. For particle 3, slightly smaller, a modest band gap of \sim 0.6 V is observed. Finally, the smallest particle (2) exhibits the largest band gap of the three, at \sim 1.2 V. The trend of increasing band gap with decreasing particle size has been shown to be valid for about 90% of Pd particles for which measurements were taken. The anomalous results that were recorded may well stem from

inaccuracies in size measurements beyond those already cited; a small Pd cluster supported on a large ‘bump’ of MgO would be difficult to distinguish from a larger particle. Also, Pd particles nucleated at certain MgO defect sites may experience electronic interactions with the substrate significant enough to impact their electronic structure measurably by this technique.

The observed trend of increasing band gap width with decreasing particle size suggests that the measured band gaps do in fact represent an intrinsic depletion of the density of states near the Fermi level, i.e. the crossover from metallic to non-metallic behavior. Nevertheless, care must be exercised in attributing such behavior to this phenomenon; alternate mechanisms can be invoked. One explanation is that the apparent band gap is attributable to a coulomb blockade. In the experiments reported here and numerous others conducted in our lab, the absence of even a single spectrum demonstrating the characteristic ‘staircase’ behavior in the I - V curve often manifested for single electron charging, seems to exclude this as a plausible explanation. Another possible explanation involves the spillover

of MgO or oxygen onto the surface of the metal particles. However, the magnitude of the observed band gaps are more consistent with quantum size effects than oxide spillover. Yet another possibility involves the electronic properties of the oxide thin film itself. Though the thin films have been shown to be electrically conductive via tunnelling to the metal single crystal substrate, if the time scale of the charge dissipation is slow, then an apparent band gap will be manifested. Experiments demonstrating that the results are unaffected by varying the tunnelling current across a wide range indicate that in fact electronic charge dissipation on our films is a fast process under these conditions. Taken together, this evidence strongly suggests that the apparent band gap indeed arises from quantum size effects [33,57–59].

These results demonstrate the viability of the technique as a means of investigating electronic properties in supported metal systems, a powerful complement to traditional photoelectronic and photoemission spectroscopies.

3.3. Catalytic properties

3.3.1. Ethane hydrogenolysis over Ni

The hydrogenolysis of alkanes over Ni has been shown to be a structure sensitive reaction. Reaction kinetics studies over Ni single crystals have shown the close packed (111) surface to be significantly less active than the more open (100) face. Similarly, studies over supported catalysts have revealed a pronounced activity enhancement (on a per surface site basis) for smaller particles relative to larger ones, down to a critically small particle size where a dramatic activity drop-off is observed [6,60–62].

This structure sensitivity is illustrated by the Arrhenius plots for ethane hydrogenolysis over Ni single crystals in Fig. 10. In addition to the obvious activity enhancement over the (100) relative to the (111) surface, a distinct difference in activation energies (24 vs. 46 kcal/mol respectively) indicates different primary reaction mechanisms for the two surfaces. Several

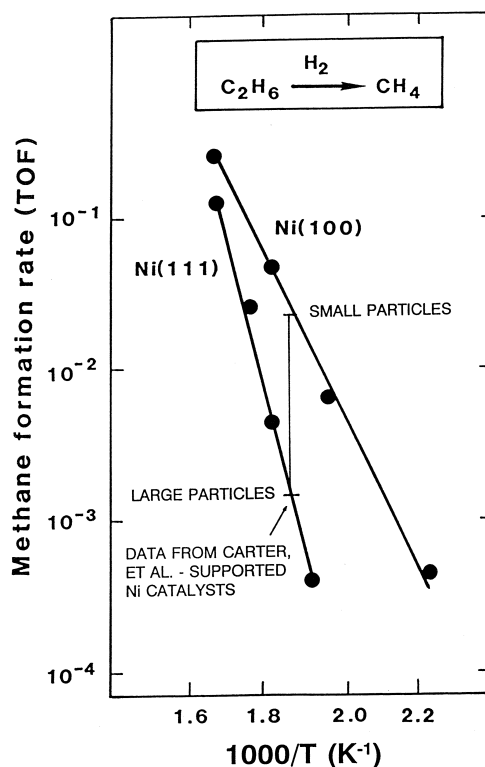


Fig. 10. Arrhenius plots for ethane hydrogenolysis over Ni(111) and (100) acquired at 100 Torr total reactant pressure at an $H_2:C_2H_6$ ratio of 100:1. The reference to supported catalyst rates is from Carter et al. [61].

explanations for this have been advanced, invoking both electronic [63] and steric effects [6,64]. For example, the higher lying electronic orbitals associated with Ni(100) might reasonably be expected to more effectively facilitate carbon–carbon bond scission relative to the (111) surface through the enhanced degree of back-donation into the antibonding orbitals of ethane.

On the other hand, it has been proposed that steric considerations are in fact the critical element determining activity in this example, and specifically, that the large distance ($\sim 2.5 \text{ \AA}$) between the highly coordinated four-fold hollow sites on the (100) surface more effectively stabilizes the carbon–carbon intermediate (exhibiting a bond length 1.3 to 1.5 \AA) for bond breaking, lowering the activation barrier for this reaction pathway. The observed structure sensitivity,

therefore, is still the result of facile C–C bond scission on the (100) surface relative to the (111), as asserted in the previous explanation, but arises from geometric rather than electronic effects. For this surface then, the rate determining step is the hydrogenation of the resulting stable carbidic or partially hydrogenated carbonaceous species. The 24 kcal/mol activation energy on this surface further supports this; the activation energy for the CO methanation reaction, discussed below, where the hydrogenation of a single carbon intermediate is the critical step, is 25 kcal/mol. Conversely, the much higher activation energy for ethane hydrogenolysis on the (111) surface is suggestive of C–C bond scission as rate limiting [6,65].

The correlation between the activity data acquired for the single crystals with previous results from supported catalysts is indicated in Fig. 10; the smaller particles display activities similar to the Ni(100) surface, while the larger particles reflect the activity of the (111) surface. Fig. 11 further illustrates this correlation; the catalyst particles are assumed to exist as regular polyhedra, fully comprised of $\langle 111 \rangle$ and $\langle 100 \rangle$

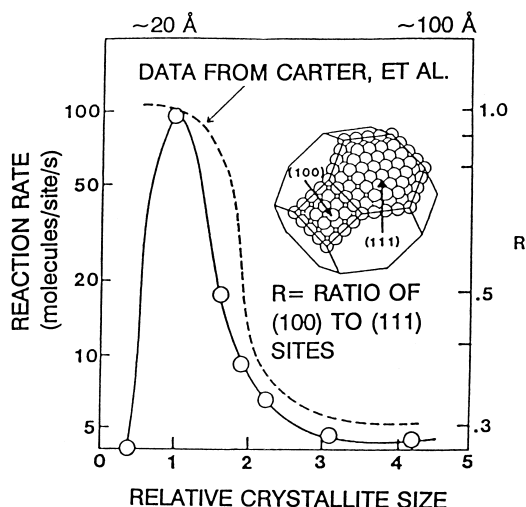


Fig. 11. Calculated activity data for a hypothetical Ni catalyst consisting of regular polyhedra comprised fully of $\langle 100 \rangle$ and $\langle 111 \rangle$ facets, based on the rate data for single crystals in Fig. 10. The ratio of $\langle 100 \rangle$ to $\langle 111 \rangle$ surface area (R) is plotted as a function of particle size. The dashed line represents experimental results for supported Ni catalysts from Goodman [6].

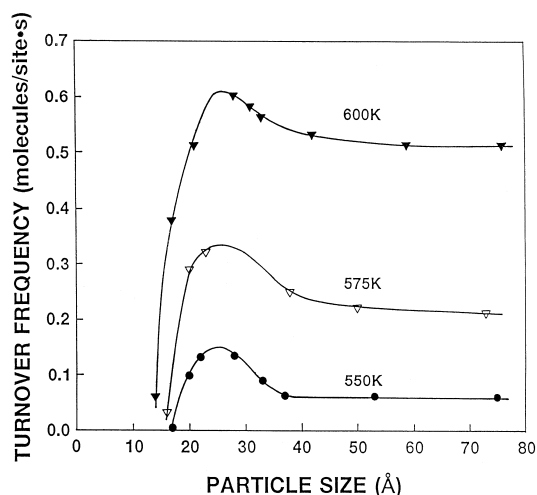


Fig. 12. Ethane hydrogenolysis activities as a function of average Ni particle size in a Ni/SiO₂/Mo(100) model catalyst at 550, 575, and 600 K, in the following reactant partial pressures: $P_{\text{H}_2} = 20$ Torr, $P_{\text{ethane}} = 1$ Torr [39].

facets. The value R is the ratio of (100) surface area to (111) surface area for the given shape, plotted as a function of particle size. The solid curve represents the theoretical activity as a function of particle size (and R), based on the activity data from the (111) and (100) single crystals in Fig. 10. This curve agrees well with data collected for high surface area supported Ni catalysts from Carter et al. [61], suggesting that the size dependence for ethane hydrogenolysis observed for supported Ni particles is closely related to the relative percentages of $\langle 100 \rangle$ and $\langle 111 \rangle$ facets comprising the surface of the particles. The activity drop-off for particles smaller than 10 Å reflects the dramatic decrease in the four-fold site population in the small particle limit (an ensemble effect) [6].

These studies were extended to include planar model supported Ni/SiO₂ catalysts. The ethane hydrogenolysis activity as a function of average particle size is shown in Fig. 12. These results clearly reflect the single crystal and supported catalyst data presented in Figs. 10 and 11, with an increase in activity with increasing particle size up to a maximum at 25 Å, and a subsequent decrease in activity as the particle size continues to increase. Above ~ 40 Å a

particle size independent constant activity is reached. A similar trend was observed in the activation energies, with the 25 Å particles exhibiting an activation energy of about 30 kcal/mol, while the larger, less active particles displayed a value of ~ 40 kcal/mol [39].

While several possibilities could account for the sharp activity decrease below an average particle size of 25 Å, including particle size dependent electronic modifications and/or increasing contributions from the metal-support interaction in the small particle limit, the close agreement with the model in Fig. 11 suggests an ensemble size effect is the critical factor in the activity drop-off. Comparing this activity data to IRAS results from the same model catalysts using CO as a probe molecule, a correlation between activity for the ethane hydrogenolysis reaction and the percentage of the total absorbance represented by the bridge-bound CO in the IRAS experiment as a function of particle size is apparent, as depicted in Fig. 13, again suggesting the requirement of an ensemble with a critical minimum size [39].

3.3.2. CO methanation over Ni / SiO

CO methanation has also been studied over planar model supported Ni/SiO₂/Mo(110) cat-

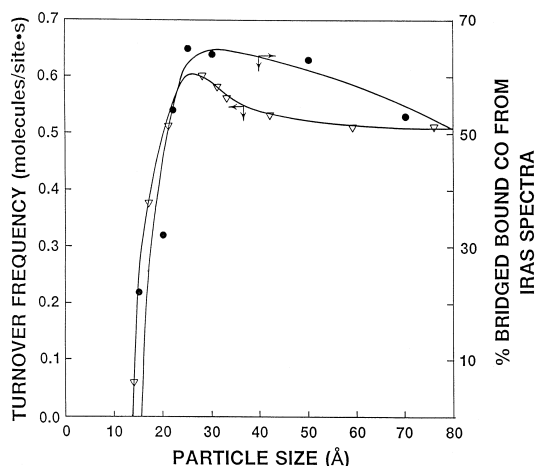


Fig. 13. Correlation between ethane hydrogenolysis activity and bridge-bound CO intensity (from IRAS in Fig. 5) as a function of average Ni particle size in Ni/SiO₂/Mo(100) [39].

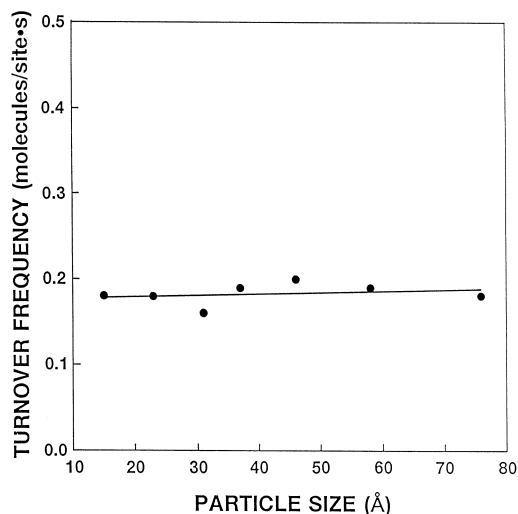


Fig. 14. CO methanation activity over Ni/SiO₂/Mo(100) as a function of Ni particle size at 600 K, in the following reactant partial pressures: $P_{H_2} = 20$ Torr, $P_{CO} = 1$ Torr [39].

alysts. The structure insensitivity of this reaction has been amply demonstrated in studies employing both single crystals [66,67] and high surface area supported Ni/SiO₂ catalysts [68,69]. The activity data acquired here for the model supported catalyst corroborates the earlier experiments, exhibiting constant activity within experimental error across a range of particle sizes (Fig. 14). Furthermore, the excellent agreement in absolute activity rates between the model catalysts, single crystals, and supported Ni powder catalysts, illustrated in Fig. 15, indicates the validity of the planar supported systems as representative models of high surface area supported catalysts [39]. The absence of structure sensitivity for this reaction, even down to very small particles, suggests that a relatively small ensemble size (perhaps only a single Ni atom) is adequate to catalyze the hydrogenation of the surface carbon intermediate.

3.3.3. CO + NO over Pd

A combined study of the CO + NO reaction over Pd has been performed utilizing single crystals, planar model supported

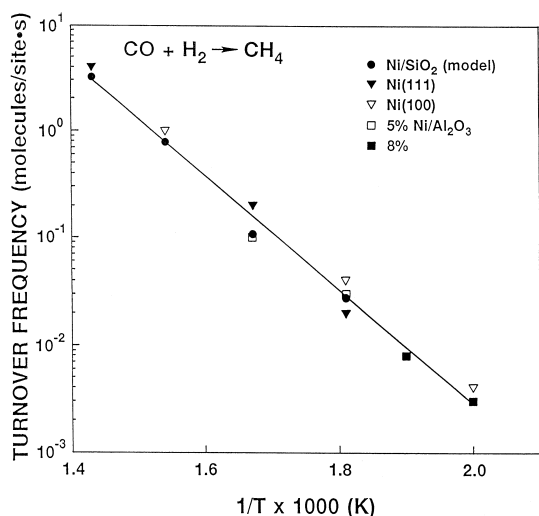


Fig. 15. Comparisons of CO methanation activities over Ni single crystals, planar model supported Ni/SiO₂/Mo(100), and conventional high surface area supported Ni/Al₂O₃ catalysts [39,68,69].

Pd/Al₂O₃/Ta(110) catalysts, and conventional high surface area Pd/Al₂O₃ powders. Fig. 16 shows activity data for each type of catalyst. A clear structure dependence is apparent. The single crystal results reveal a five-fold activity enhancement for the Pd (111) surface compared to the more open (100) and (110) faces [31,70] (the (110) data is not shown). For the Pd/Al₂O₃ powder catalysts, an even more dramatic effect is seen. The catalyst supporting the ~1200 Å particles displays a 30-fold activity enhancement relative to the catalyst supporting ~60 Å particles [31,71]; a similar particle size dependence has been observed for supported Rh catalysts [72]. The planar model supported catalysts exhibit the same activity trend with particle size, though to a lesser degree.

Clearly there are some differences in the behavior among the three types of catalysts. The single crystals display significantly higher activities and lower activation energies relative to the supported catalysts. A similar discrepancy between single crystal and supported catalyst results have been observed over Rh [72,73]. Nevertheless, there are also similarities in the activity trends. IRAS has shown (as described above)

that larger Pd particles exhibit surface morphologies dominated by low index <111> and <100> type faceting, while the smaller particles are characterized by less well defined faceting and a high density of step/edge defect sites. From this perspective, the observed trends are the same for the single crystals and the supported particles; close packed surfaces are more active than open ones.

For rhodium it has been suggested that the observed structure sensitivity may relate to the preferential formation and/or stabilization of an inactive atomic nitrogen species on reactive, undercoordinated (more 'open') sites more abundant on small particles. This hypothesis is largely based on particle size resolved supported Rh NO TPD studies by Altman and Gorte [74] that reveal an enhancement in a high temperature N₂ recombinative desorption feature with decreasing particle size (and decreasing activity). In order to test the applicability of this model to

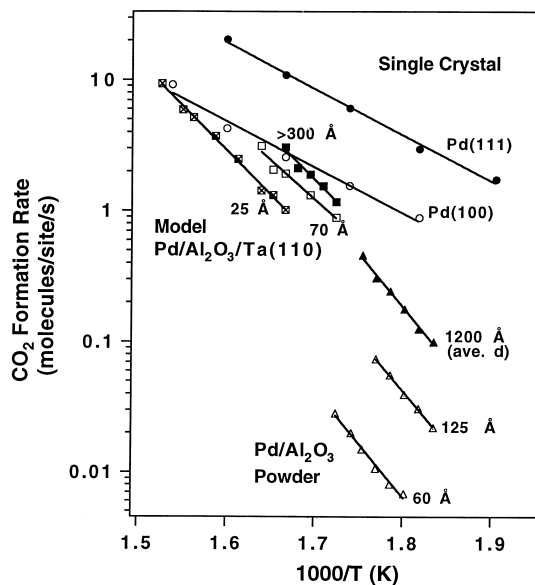


Fig. 16. CO+NO Arrhenius plots for single crystals, model planar supported, and Pd/Al₂O₃ powder catalysts. The powder catalyst data were taken in the flow reaction mode (4.4/5.2 Torr CO/NO) and the model catalyst and single crystal data were acquired for a batch reaction in 1 Torr of each reactant. Activity is measured as CO₂ formation rate; Arrhenius plots based on NO reduction are qualitatively identical [31,70].

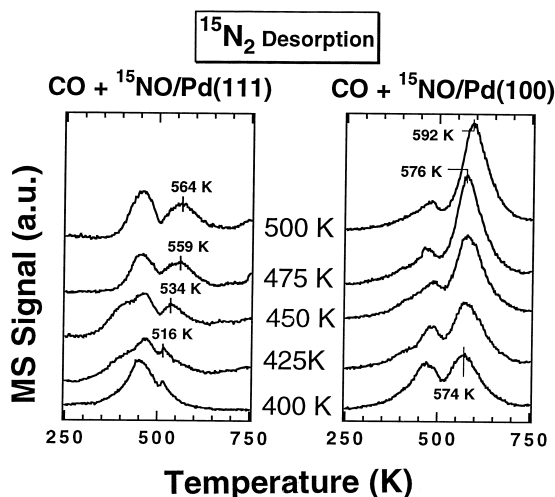


Fig. 17. TPD spectra for $^{15}\text{N}_2$ recombinative desorption after 500 L exposure to $\text{CO} + ^{15}\text{NO}$ at 1:1 ratios at the indicated substrate temperatures on Pd(111) and (100) [31,70].

Pd catalysts, analogous experiments were performed on Pd single crystals and model supported catalysts.

Fig. 17 shows N_2 TPD spectra for coadsorbed CO and ^{15}NO on the Pd (111) and (100) single crystals, after a 500 L exposure ($\text{CO} : ^{15}\text{NO}$ 1:1) at the indicated temperature, followed by cooling in the background gas. For each spectrum on both surfaces, two recombinative features appear. A low temperature feature appears at ~ 450 K, along with a higher temperature peak ranging from ~ 515 to 590 K. The ratio of the peak area of the high temperature feature to that of the low temperature feature increases with increasing exposure temperature for both surfaces.

There are also some differences; the total TPD N_2 peak area is higher on the less active (100) surface, indicating more facile dissociation of NO. Additionally, the ratio of high temperature to low temperature peak area is significantly higher for the (100) surface, particularly at the higher exposure temperatures. In fact, for the 500 K exposure, comparisons with a monolayer coverage of the atomic N on Pd(100) indicate an 80% coverage of the more

thermally stable N_a on the Pd (100) vs. a 20% coverage on the Pd(111) [70]. It is interesting to note that this enhancement for N_2 formation/stabilization is roughly inversely proportional to the activity ratios of the two surfaces.

Another important observation is that for the 500 K exposure, the desorption maximum of the high temperature feature is near the upper end of the typical temperature range employed in the reaction kinetics experiments, suggesting that this species may be inactive under these conditions. In fact, for an analogous TPD experiment using adsorbed ^{15}NO alone, though the results are qualitatively identical to the case with CO and NO coadsorbed, the maximum at each exposure temperature is shifted higher by about 30 K; this may be the more relevant measurement, particularly for the (111) surface, as in situ IRAS experiments have revealed a significant enhancement for NO adsorption relative to CO adsorption at reaction temperatures on this surface [70,75]. These TPD results suggest that the differences in activity observed for the single crystals may in fact be related to the structure sensitive formation of an inactive nitrogen species.

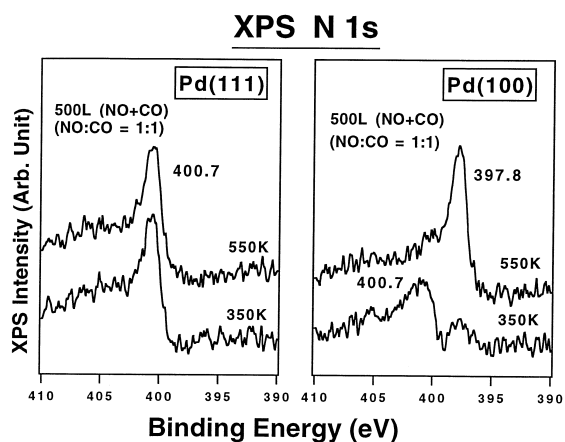


Fig. 18. XPS spectra of the N 1s peak on Pd(111) and (100) after a 500 L exposure to $\text{CO} + \text{NO}$ (1:1) at 350 and 550 K. The peak at 400.7 eV is attributed to N in molecularly bound NO_a , while the feature at 397.8 eV is assigned to atomic N_a [31].

Another indicator for the enhanced formation of the inactive N_a species on the (100) surface can be found from XPS investigation. Nitrogen 1s region XPS data are presented in Fig. 18 for the (111) and the (100) surfaces. Significant differences are apparent between them. For the (111) surface, a single peak appears at 400.7 eV, attributed to nitrogen in molecularly bound NO_a for both exposure temperatures (350 K and 550 K). For Pd(100), however, an additional peak is observed at 397.8 eV, assigned to atomic nitrogen. In fact, for the 550 K NO exposure temperature, this peak dominates the spectrum, with only a small shoulder at 400.7 eV arising from NO_a . Even for the 350 K exposure on the (100) surface, it is clear that a significant degree of NO dissociation has occurred. These results seem to unambiguously indicate that the dissociation of NO is more facile on the (100) surface.

The XPS annealing series in Fig. 19 demonstrates that the atomic nitrogen species on the

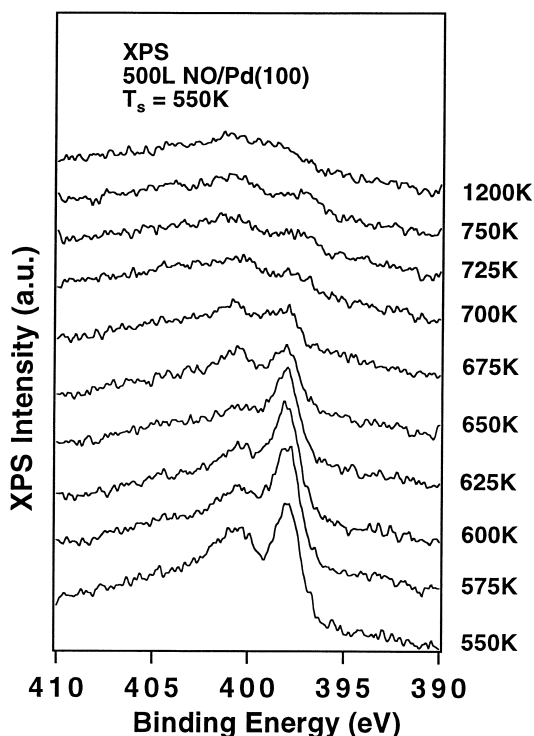


Fig. 19. XPS annealing series of the N1s peak on Pd(100) after a 500 Langmuir NO exposure at 500 K [31].

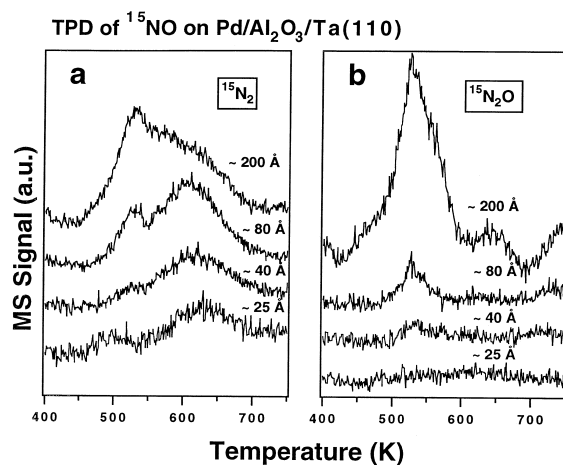


Fig. 20. TPD monitoring (a) $^{15}N_2$ desorption and (b) $^{15}N_2O$ desorption over several different Pd coverages with the indicated average particle sizes in a Pd/ Al_2O_3 /Ta(110) catalyst after exposure to 1×10^{-7} Torr ^{15}NO for 5 min at 550 K [31].

(100) surface is thermally stable up to ~ 650 K, above which the N_a peak (397.8 eV) begins to attenuate significantly. It is interesting to note that this correlates closely to the light off temperature (the critical temperature at which an exponential rate increase occurs) for the Pd(100) surface observed in this study.

Taken together, the XPS and TPD data for the single crystals provide compelling evidence for the enhanced formation of a thermally stable (at reaction temperatures) atomic nitrogen species on the Pd(100) surface relative to the (111) surface. The thermal stability of the N_a species suggests that it is inactive under reaction conditions and inhibits the reaction [31].

In order to determine if this correlation between N_a formation/stabilization and activity extends to the supported particles, a TPD experiment analogous to the type described above for the single crystals was performed over several different loadings of Pd in the Pd/ Al_2O_3 /Ta(110) model catalyst. N_2 and N_2O desorption spectra are presented in Fig. 20 for four loadings of Pd (corresponding to the average particle sizes indicated in the figure) after a 5 min exposure to 1×10^{-7} Torr of ^{15}NO at 550 K, followed by cooling to 300 K and

subsequent pump-out. The N_2 desorption spectra are qualitatively identical to those observed for the single crystals; two distinct recombinative features appear in each case. The smaller particles clearly display an enhancement for the high temperature feature relative to the low temperature feature. Another indicator of the ratio of atomic nitrogen to molecularly bound NO on the surface is the desorption of N_2O (Fig. 20b). For the 25 Å particles, the amount of N_2O produced is beneath the detection limit of the mass spectrometer. On the other hand, significant N_2O desorption occurs from the largest particles (~ 200 Å). This enhancement for N_2O production for larger particles is clearly demonstrated by a comparison of the desorption peak areas between the traces for the 40 Å particles in the 2 ML loading, and the 200 Å particles in the 22 ML loading; though the total metal surface area differs by only a factor of ~ 2 , N_2O production is in fact about eight times greater for the 200 Å particles. This implies a lower ratio of atomic N_a to molecularly bound NO_a on the surface with increasing particle size (and activity). This correlation again suggests that catalyst activity is heavily influenced by the structure sensitive propensity for N_a formation and stabilization for the CO + NO reaction over Pd.

These observations alone may not be sufficient to explain the overall differences in absolute activity and activation energy observed between the single crystals and the supported catalysts. However, the high density of undercoordinated, reactive sites on the supported catalysts that seems to influence the formation of the stable inactive species, may have other effects as well; it has been observed that small supported Pd particles can dissociate CO under certain conditions, even though no analogous behavior has been observed on single crystals [36,76–78].

3.3.4. Cyclotrimerization of acetylene over Pd

The cyclotrimerization of acetylene to benzene over Pd has been shown by single crystal

investigations to be structure sensitive, with the (111) face exhibiting the highest activity (compared to (100) and (110) surfaces) [79–83] at low pressures. Isotopic labelling experiments have indicated that the reaction most likely occurs without C–C bond scission [84]; a penta-diene metallocycle has been proposed as the reaction intermediate [85,86]. This explanation is supported by studies indicating that small yields of furan [87] or thiophene [88] are reactively formed with acetylene over Pd in the presence of oxygen or sulfur.

Benzene TPD results from Pd(111) following low temperature acetylene adsorption (< 200 K) reveal two distinct desorption features at ~ 250 K and ~ 500 K. The high temperature feature has been attributed to benzene bound flat on the metal surface, while the low temperature desorption maximum arises from benzene in an ordered, compressed overlayer, bound weakly in a tilted configuration. A third desorption maximum near 380 K has been observed on Pd(100) [89–91], and in one case on the (111) surface [89]. The appearance of this feature has alternately been attributed to desorption from a close packed, flat-bonded benzene overlayer or to benzene bound in surface defect sites.

The observed structure sensitivity has been rationalized in terms of an ensemble effect, where the geometry of the hexagonally packed (111) surface favors the formation of benzene. This has been addressed in bimetallic studies utilizing Au/Pd(111), Pd/Au(111), and Au/Pd colloid particles, to gauge the effect of breaking up the Pd ensembles. It was concluded that an ensemble of seven Pd atoms, or six Pd atoms surrounding a central Au atom, is required for benzene formation from acetylene. In fact, the ensemble with the central Au atom was found to be more effective for benzene formation, possibly because benzene is more weakly bound on this surface, favoring benzene desorption (rather than decomposition) relative to pure Pd [92–94].

If the structure sensitivity observed for the single crystals is indeed attributable to an ensemble effect, this might reasonably be ex-

pected to be manifested as a particle size dependence favoring larger particles in supported catalysts. TPD experiments were performed on planar model supported catalysts to investigate this possibility.

Benzene TPD results for the supported particles are very similar to the analogous low index single crystal results [95]. Fig. 21 illustrates that three distinct desorption features are apparent across a range of Pd loadings in planar model supported Pd/Al₂O₃/Mo(110) catalysts; a low temperature feature at 270 K, an intermediate feature at 370 K, and a high temperature peak at 530 K. Comparisons of the TPD results reveal distinct particle size effects. For the smallest

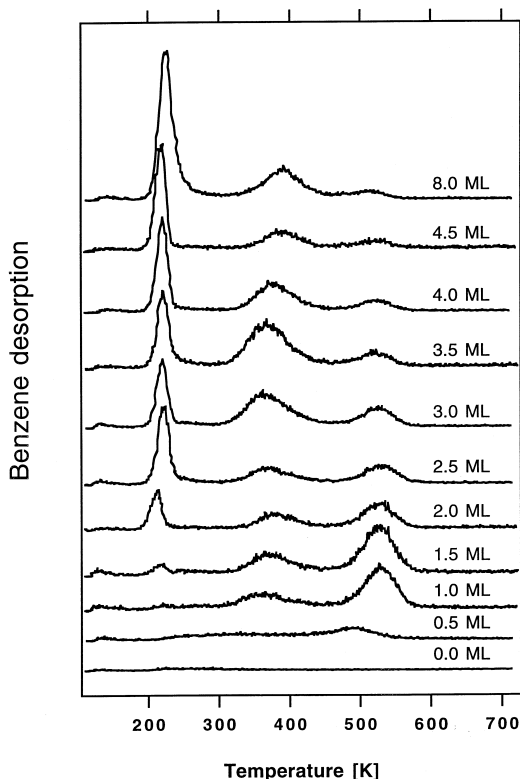


Fig. 21. Benzene TPD from supported Pd particles in Pd/Al₂O₃/Mo(110) model catalysts following a 70 L acetylene exposure at 150 K at the indicated metal loadings. Based on comparisons with TPD data, average Pd particle sizes range from ~ 100 Å for the 8 ML coverage to less than 20 Å for 0.5 ML coverage [95].

particles (~ 15 – 20 Å d_{ave}), most of the benzene desorption occurs above 500 K, with very little low temperature benzene evolution. As the particle size is increased, the high temperature peak begins to attenuate, while the desorption peak at 230 K increases in intensity. For Pd loadings ≥ 4 ML (average particle size ≥ 50 Å), the low temperature desorption pathway is clearly favored. This will be discussed in detail below.

Several other interesting observations can be made for this data set. First of all, a substantial decrease in benzene production is observed between the 1.0 ML and 0.5 ML Pd coverages; the TPD peak area decreases by about a factor of four going from the higher to the lower Pd coverage, even though the Pd surface area is decreasing by just under a factor of two. This marked drop-off in activity at the extreme lower end of the particle size range studied (average particle diameter ~ 15 Å, with a significant fraction of even smaller particles in the lower wing of the distribution) suggests the manifestation of the anticipated ensemble effect.

Another point of interest involves the desorption peak at 370 K; the presence of this feature on the supported particles suggests that it is probably related to benzene adsorbed at defect sites. In fact, this feature is suppressed to a greater degree than the other desorption maxima upon iterative reaction runs, consistent with having preferential build-up of inactive carbon on reactive defects. That surface decomposition is one (or one group) of the reaction pathways available for the benzene formed at low temperatures is demonstrated by the evolution of smaller hydrocarbons between 230 K and 320 K observed for every Pd loading studied.

Intuitively then, if the feature at 370 K is in fact related to benzene adsorbed at defect sites, one might expect to see the ratio of this feature to the other desorption features in the TPD traces increase with decreasing particle size. The behavior actually observed, however, is quite different. A relatively small contribution from the 370 K peak compared to the high

temperature peak is observed for the smallest particles. The ratio increases as the contribution from the high temperature peak diminishes with increasing particle size up until a Pd coverage of ~ 3.5 ML, where a maximum is reached. Above this coverage, the ratio starts to decline again as the low temperature peak gains in intensity, and the 370 K peak attenuates. Apparently, then, the relative contribution from this feature is only partly influenced by the density of surface defects. Perhaps both of the explanations advanced to explain this feature for single crystals (discussed above) are valid, and there is a convolution of the two effects. Alternatively, perhaps the smaller particles favor the decomposition reaction at the lower temperature, deactivating the defect sites for benzene adsorption. This is an interesting issue that warrants further study.

Returning to the observation that the larger particles favor the low temperature reaction pathway, there are a couple of ways to interpret this. Assuming regular polyhedra comprised exclusively of $\langle 111 \rangle$ and $\langle 100 \rangle$ facets, the ratio of the former to the latter increases with increasing particle size, as has been illustrated above for Ni. Single crystal TPD studies of Pd(111) and (100) have revealed a similar enhancement for the low temperature desorption on the (111) surface [83]. Therefore, this effect may well be related to the ratio of $\langle 111 \rangle$ facets on the surface. An alternate explanation invokes the enhanced curvature of the smaller particles that precludes the degree of compression in the benzene overlayer that results in the tilted, weakly bound configuration.

These results may also have implications for reaction activity under equilibrium conditions. The reactively formed benzene in the tilted configuration in the compressed overlayer has several reaction pathways available to it, including desorption, decomposition, and transition to the strongly flat bound species. While a definitive enhancement for benzene evolution was not observed for the larger particles in the TPD experiments, the data suggest an activity depen-

dence nonetheless. Generally, one would expect an enhanced propensity for low temperature desorption to likewise enhance the rate of benzene formation in a reaction equilibrium situation. Single crystal studies by Rucker et al. that point to benzene desorption as the rate determining step lend further support to this viewpoint. For Pd single crystals at atmospheric pressures under batch reaction conditions, the (111) surface is more reactive than the (100) surface if corrections are made for site blocking by inactive carbon [83]. In fact, Ormerod and Lambert have shown that larger Pd particles in conventional supported catalysts are more active [96].

In this interpretation then, the lower activities for the smaller particles is not due to a critical size ensemble effect (except for the extremely small particles exhibiting the dramatic intensity drop-off), but rather to the enhanced curvatures and absence of large, $\langle 111 \rangle$ terraces. These characteristics preclude the formation of the ordered compressed overlayer of reactively formed benzene weakly bound in the tilted configuration, and favor the more strongly adsorbed flat bonded benzene. Also, the smaller particles with their higher densities of defects may favor the low temperature decomposition reaction, as suggested by the attenuation of the benzene peak at 370 K associated with defects.

While these low temperature adsorption, low pressure experiments reveal interesting particle size effects, it is difficult (and perhaps dangerous) to attempt to extrapolate these results to the high pressure, high temperature situation in a conclusive way. Changes in surface coverages of reactants and poisons can have profound effects on reaction mechanisms, as shown by the single crystal work (Rucker et al. [83]). Ideally, these experiments must be expanded to include high temperature, high pressure reaction kinetics. Nevertheless, these results [95] provide yet another example of the excellent utility and scope associated with these unique model catalysts for investigation of heterogeneous catalytic processes.

4. Conclusions

Clearly, the employment of planar model supported catalysts in characterization and reaction kinetics studies affords unique research opportunities in the area of heterogeneous catalysis science. Because these samples address important issues such as the metal-support interaction and the intrinsic effects of particle size, while featuring many of the characteristics which render single crystals so eminently suited to atomic level investigation using conventional UHV-based analytical techniques, their incorporation into such studies represents a perfect complement to the more traditional methodology. Investigations regarding chemical/electronic and physical/structural properties can be performed for the supported particles in the model catalyst at a level of detail unlikely to be achieved for the analogous high-surface area counterparts.

The experiments described here provide a broad illustration of the utility and versatility of these unique and fascinating systems, establishing their study as a viable and promising approach to catalyst characterization and elucidation of catalytic processes at the most fundamental level.

Acknowledgements

We acknowledge with pleasure the support of these efforts by the Department of Energy, Office of Energy Sciences, Division of Chemical Sciences and the Robert A. Welch Foundation.

References

- [1] R.C. Baetzold, J.F. Hamilton, *Prog. Solid State Chem.* 15 (1983) .
- [2] H. Poppa, *Vacuum* 34 (1984) 1081.
- [3] M.G. Mason, *Phys. Rev. B* 27 (1982) 748.
- [4] Z. Bastl, *Vacuum* 36 (1986) 447.
- [5] W.G. Durrer, H. Poppa, J.T. Dickinson, C. Park, *J. Vac. Sci. Technol. A* 3 (1985) 1545.
- [6] D.W. Goodman, *Catal. Today* 12 (1992) 189.
- [7] P.J. Berlowitz, C.H.F. Peden, D.W. Goodman, *J. Phys. Chem.* 92 (1988) 5213.
- [8] J. Szanyi, D.W. Goodman, *Rev. Sci. Instrum.* 64 (1993) 2350.
- [9] R.A. Campbell, D.W. Goodman, *Rev. Sci. Instrum.* 63 (1992) 172.
- [10] B.A. Sexton, G.A. Somorjai, *J. Catal.* 46 (1977) 167.
- [11] H.P. Bonzel, H.J. Krebs, *Surf. Sci.* 91 (1980) 499.
- [12] D.W. Goodman, R.D. Kelley, T.E. Madey, J.T. Yates Jr., *J. Catal.* 63 (1980) 226.
- [13] C.T. Campbell, M.T. Paffett, *Surf. Sci.* 139 (1984) 396.
- [14] J.A. Rodriguez, D.W. Goodman, *Surf. Sci. Rep.* 14 (1991) 1.
- [15] D.W. Goodman, *Annu. Rev. Phys.* 37 (1986) 425.
- [16] D.W. Goodman, *Surf. Sci.* 299/300 (1994) 837.
- [17] M.A. Vannice, R.L. Garten, *J. Catal.* 56 (1979) 536.
- [18] D.W. Goodman, *Surf. Rev. Lett.* 2 (1995) 9.
- [19] C. Xu, D.W. Goodman in: G. Ertl, H. Knozinger, J. Weitkamp (Eds.), *Handbook Heterogeneous Catalysis*, VCH, Weinheim, 1996.
- [20] S.C. Street, C. Xu, D.W. Goodman, *Annu. Rev. Phys. Chem.* 48 (1997) 37.
- [21] D.R. Rainer, D.W. Goodman, in: R.M. Lambert, G. Pacchioni (Eds.), *Chemisorption and Reactivity on Supported Clusters and Thin Films*, Kluwer Academic Publishers, 1997, p. 27.
- [22] D.W. Goodman, *Chem. Rev.* 95 (1995) 523.
- [23] M.-C. Wu, D.W. Goodman, *J. Phys. Chem.* 98 (1994) 9874.
- [24] P.J. Chen, D.W. Goodman, *Surf. Sci. Lett.* 312 (1994) L767.
- [25] J.-W. He, X. Xu, J.S. Corneille, D.W. Goodman, *Surf. Sci.* 279 (1992) 119.
- [26] X. Xu, D.W. Goodman, *Appl. Phys. Lett.* 61 (7) (1992) 774.
- [27] H.R. Phillip, *J. Phys. Chem. Solids* 32 (1971) 1935.
- [28] X. Xu, D.W. Goodman, *Surf. Sci.* 282 (1993) 323.
- [29] S. Ladas, H. Poppa, M. Boudart, *Surf. Sci.* 102 (1981) 151.
- [30] X. Xu, D.W. Goodman, *J. Phys. Chem.* 97 (1993) 7711.
- [31] D.R. Rainer, S.M. Vesecky, M. Koranne, W.S. Oh, D.W. Goodman, *J. Catal.* 167 (1997) 234.
- [32] D.R. Rainer, C. Xu, D.W. Goodman, *J. Mol. Catal. A.* 1453 (1997) in press.
- [33] C. Xu, W.S. Oh, G. Liu, D.Y. Kim, D.W. Goodman, *J. Vac. Sci. Technol. A* 15 (3) (1997) 1755.
- [34] F.M. Hoffman, *Surf. Sci. Rep.* 3 (1983) 107.
- [35] J. Szanyi, W.K. Kuhn, D.W. Goodman, *J. Vac. Sci. Technol. A* 11 (1993) 1969.
- [36] D.R. Rainer, M.-C. Wu, D.I. Mahon, D.W. Goodman, *J. Vac. Sci. Technol. A* 14 (1996) 1184.
- [37] X. Xu, J. Szanyi, Q. Zu, D.W. Goodman, *Catal. Today* 21 (1994) 57.
- [38] C.R. Henry, C. Chapon, C. Goyhenex, R. Minot, *Surf. Sci.* 272 (1992) 283.
- [39] K. Coulter, X. Xu, D.W. Goodman, *J. Phys. Chem.* 98 (1994) 1245.
- [40] P. Hollins, J. Pritchard, in: A.T. Bell, M.L. Hair (Eds.), *Vibrational Spectroscopies for Adsorbed Species*, ACS Symp. Ser. 137, American Chemical Society, Washington, DC, 1980.
- [41] P. Hollins, *Surf. Sci. Rep.* 16 (1992) 51.
- [42] D.R. Rainer, C. Xu, P.M. Holmblad, D.W. Goodman, *J. Vac. Sci. Technol. A* 15 (3) (1997) 1653.

- [43] S.H. Lu, J. Yao, L. Zhu, G.L. Liu, F.Q. Liu, S.C. Wu, *Phys. Rev. B* 45 (1992) 6142.
- [44] H.A.C.M. Hendrickx, V. Ponc, *Surf. Sci.* 192 (1987) 234.
- [45] D.R. Rainer, J.S. Corneille, D.W. Goodman, *J. Vac. Sci. Technol. A* 13 (1995) 1595.
- [46] P.M. Holmblad, D.R. Rainer, D.W. Goodman, to be published.
- [47] G.K. Wertheim, S.B. DiCenzo, *Phys. Rev. B* 37 (1988) 844.
- [48] S.B. DiCenzo, G.K. Wertheim, *Comments Solid State Phys.* 11 (1985) 203.
- [49] S. Kohiki, S. Ikeda, *Phys. Rev. B* 34 (1986) 3786.
- [50] F. Parmigiani, E. Kay, P.S. Bagus, C.J. Neline, *J. Electron Spectrosc. Relat. Phenom.* 36 (1985) 257.
- [51] T.T.P. Cheung, *Surf. Sci.* 140 (1984) 151.
- [52] Z. Basl, *Vacuum* 36 (1986) 447.
- [53] M.G. Mason, *Phys. Rev. B* 27 (1983) 748.
- [54] W.F. Egelhoff Jr., G.G. Tibbetts, *Phys. Rev. B* 19 (1979) 5028.
- [55] X. Xu, D.W. Goodman, *J. Phys. Chem.* 97 (1993) 683.
- [56] M.-C. Wu, C.M. Truong, D.W. Goodman, *Phys. Rev. B* 46 (1992) 12688.
- [57] C. Xu, D.W. Goodman, *Chem. Phys. Lett.* 263 (1996) 13.
- [58] P.N. First, J.A. Stroschio, R.A. Dragoset, D.T. Pierce, R.J. Celotta, *Phys. Rev. Lett.* 63 (1989) 1416.
- [59] M. Suzuki, T. Fukuda, *Phys. Rev. B* 44 (1991) 3187.
- [60] D.W. Goodman, *Surf. Sci. Lett.* 123 (1982) L679.
- [61] J.L. Carter, J.A. Cusumano, J.H. Sinfelt, *J. Phys. Chem.* 70 (1966) 2257.
- [62] G.A. Martin, *J. Catal.* 60 (1979) 452.
- [63] M.C. Desjonqueres, F. Cyrot-Lackmann, *J. Chem. Phys.* 64 (1976) 3707.
- [64] M. Kiskinova, D.W. Goodman, *Surf. Sci.* 108 (1981) 64.
- [65] D.W. Goodman, R.D. Kelley, T.E. Madey, J.M. White, *J. Catal.* 64 (1980) 479.
- [66] D.W. Goodman, *Acc. Chem. Res.* 17 (1984) 194.
- [67] R.D. Kelley, D.W. Goodman, *Surf. Sci. Lett.* 123 (1982) L743.
- [68] M.A. Vannice, *J. Catal.* 44 (1976) 152.
- [69] M.A. Vannice, *Catal. Rev. Sci. Eng.* 14 (1976) 153.
- [70] S.M. Vesecky, D.R. Rainer, D.W. Goodman, *J. Vac. Sci. Technol. A* 14 (1996) 1457.
- [71] D.R. Rainer, M. Koranne, S.M. Vesecky, D.W. Goodman, *J. Phys. Chem.*, in press.
- [72] S.H. Oh, C.C. Eickel, *J. Catal.* 128 (1991) 526.
- [73] B.K. Cho, *J. Catal.* 131 (1991) 74.
- [74] E.I. Altman, R.J. Gorte, *J. Catal.* 113 (1988) 185.
- [75] X. Xu, P.J. Chen, D.W. Goodman, *J. Phys. Chem.* 98 (1994) 9242.
- [76] V. Matolin, E. Gillet, *Surf. Sci.* 75 (1990) 238.
- [77] M.H. El-Yakhoulfi, E. Gillet, *Catal. Lett.* 17 (1993) 11.
- [78] E. Gillet, S. Channokhone, V. Matolin, *J. Catal.* 97 (1986) 437.
- [79] W.T. Tysoe, G.L. Nyberg, R.M. Lambert, *Surf. Sci.* 135 (1983) 128.
- [80] W.T. Tysoe, G.L. Nyber, R.M. Lambert, *J. Chem. Soc., Chem. Commun.*, (1983) 623.
- [81] W. Sesselmann, B. Woratschek, G. Ertl, J. Küppers, H. Haberland, *Surf. Sci.* 130 (1983) 245.
- [82] T.M. Gentle, E.L. Muetterties, *J. Phys. Chem.* 87 (1983) 2469.
- [83] T.J. Rucker, M.A. Logan, T.M. Gentle, E.L. Muetterties, G.A. Somorjai, *J. Phys. Chem.* 90 (1986) 2703.
- [84] C.H. Patterson, R.M. Lambert, *J. Phys. Chem.* 92 (1988) 1266.
- [85] C.H. Patterson, J.M. Mundenar, P.Y. Timbrell, A.J. Gellman, R.M. Lambert, *Surf. Sci.* 208 (1989) 93.
- [86] G. Pacchioni, R.M. Lambert, *Surf. Sci.* 304 (1994) 208.
- [87] R.M. Ormerod, R.M. Lambert, *Catal. Lett.* 6 (1990) 121.
- [88] A.J. Gellman, *Langmuir* 7 (1991) 827.
- [89] W.T. Tysoe, G.L. Nyberg, R.M. Lambert, *J. Phys. Chem.* 90 (1986) 3188.
- [90] W.T. Tysoe, R.M. Ormerod, R.M. Lambert, G. Zgralich, A. Ramirez-Cuesta, *J. Chem. Phys.* 97 (1993) 3365.
- [91] R.M. Ormerod, C.J. Baddeley, R.M. Lambert, *Surf. Sci. Lett.* 259 (1991) L709.
- [92] C.J. Baddeley, M. Tikhov, C. Hardacre, J.R. Lomas, R.M. Lambert, *J. Chem. Phys.* 100 (1996) 2189.
- [93] A.F. Lee, C.J. Baddeley, C. Hardacre, R.M. Ormerod, R.M. Lambert, *J. Phys. Chem.* 99 (1995) 6096.
- [94] C.J. Baddeley, R.M. Ormerod, A.W. Stevenson, R.M. Lambert, *J. Chem. Phys.* 99 (1995) 5146.
- [95] P.M. Holmblad, D.R. Rainer, D.W. Goodman, *J. Phys. Chem.*, submitted.
- [96] R.M. Ormerod, R.M. Lambert, *J. Chem. Soc., Chem. Commun.*, (1990) 1421.
- [97] A. Rochefort, M. Abon, P. Delichere, J.C. Bertolini, *Surf. Sci.* 294 (1993) 43.